49th AIAA Aerospace Sciences Meeting including the New Horizons Forum and Aerospace Exposition
4 - 7 January 2011, Orlando, Florida

AIAA 2011-1297

Delayed Detached Eddy Simulation of a Stall Flow Over NACA0012 Airfoil Using High Order Schemes

Hong-Sik IM [*], Ge-Cheng Zha[†]
Dept. of Mechanical and Aerospace Engineering
University of Miami
Coral Gables, Florida 33124
E-mail: gzha@miami.edu

Abstract

Delayed-Detached Eddy Simulation (DDES) is conducted to simulate aerodynamic stall flow over NACA0012 airfoil at 45° angle of attack. DDES is an improved version of DES97 to avoid Modeled-Stress Depletion (MSD) in attached boundary layer by redefining the length scale of DES97. The test of DDES for the flat plate shows that the delayed LES function facilitates DDES to preserve eddy viscosity even with a severe grid that makes DES to undergo MSD. For comparison, DES97 and URANS also were conducted for the stalled NACA 0012 airfoil flow. DDES and DES predicted the drag coefficient accurately, while URANS overpredicted the drag by 33.6%. Both DES and DDES appear to be satisfactory to simulate the stalled airfoil flow at high angle of attack, in which the large structure of vortex are dominant.

1 Introduction

Dynamic stall is an unsteady instability typically associated with flow separation. The stall vortex is formed around its leading edge and travels along the airfoil surface as it grows, and finally separates from the airfoil surface near the trailing edge. Instability of dynamic stall grows with flow separation and eventually prevents the wing's ability to create lift toward the dynamic stall.

Stall flow simulation has many difficulties by using Reynolds-averaged Navier-Strokes (RANS) methods due to unsteady vortical flows. RANS methods intend to model the large scale eddies using a universal model. Large scale turbulence is affected by the flow geometry and boundary conditions and a universal model does not exist.

Large Eddy Simulation (LES) is promising to overcome the disadvantages of the RANS model. In LES, the governing equations are spatially filtered on the scale of the numerical grid. The large energy containing scales are directly simulated, and the small scale eddies, which are generally more homogeneous and universal, are modeled. The large eddies are strongly affected by the flow field geometry boundaries. Therefore the direct computation of the large eddies by LES is more accurate than the modeling of the large eddies by RANS. However, to resolve the wall boundary layer, LES needs the CPU resource not much less than the Direct Numerical Simulation(DNS). For engineering applications, it is not hopeful for LES to be rigorously used until in another 4 decades[1].

To overcome the intensive CPU requirement for LES, Spalart et al. developed the detached eddy simulation (DES) strategy[1], which is a hybrid RANS and LES method. Near the solid surface within the wall boundary layer, the unsteady RANS model is realized. Away from the wall surface, the model automatically converts to LES. By using the RANS model near walls, the mesh size as well as the CPU time can be tremendously reduced. The motivation of DES is that the LES is powerful in regions of massive separation and other free shear flows such as jets, but much too costly in the large area of thin wall boundary layers.

However, a defect of the first generation DES model, DES97, has been also exposed. DES97 may behave incorrectly in the regions of thick boundary layers and shallow separation regions due to the grid spacing dependence[2]. Delayed detached-eddy simulation (DDES) by Spalart[2] is an improved version of the original DES97 model. With DDES, a blending function similar to the one used by Menter and Kuntz [3] for the SST model is introduced to limit the length scale of DES97 to ensure the transition of RANS to LES be independent of grid spacing. Spalart et al.[2]

---

[*] Graduate Student, AIAA Member
[†] Associate Professor, AIAA Senior Member

validated DDES for a flat plate with the wall-parallel grid spacing about 1/10th of the boundary layer thickness (severe grid or ambiguous grid defined by Spalart).

Numerical studies on the dyanamic stall has been widely performed by other researchers[4, 5, 6, 7]. For example, Morton et al.[4] applied DES97 for simulating the full aircraft experiencing massively separated flows. The F/A-18E simulations demonstrated the ability of DES to accurately predict transonic nonlinear aerodynamic phenomena of abrupt wing stall, which is created by a shock-vortex-boundary layer interaction. The predicted lift and drag of the F-15E by RANS deviates around 10% from the experiment. Travin et al.[7] particularly confirms that for massively separated flows over NACA0021 airfoil at 60 degrees angle of attack, DDES performs quite the same as the original DES97 using a coarse grid of $141\times101\times31$ nodes in the streamwise, wall-normal and spanwise directions respectively.

For DES, the majority of the flow field with the large vortex structure of separation is resolved by LES. The requirement for DES numerical schemes hence should be as stringent as LES. To achieve high accuracy DES solution, the high order (higher than 2nd order) scheme is necessary. Travin et al. [7] has employed a high order biased upwind scheme and central differencing scheme for DES. However, the scheme is not aimed at shock capturing and has difficulty in dealing with shock boundary layer interaction of high speed flows.

This paper employs the 5th order low diffusion WENO shock capturing scheme and 4th order central differencing scheme recently developed in our group[8, 9, 10, 11]. The WENO scheme [10, 11] overcomes the smoothness estimator oscillation of the original Jiang-Shu's WENO scheme[12] and achieves higher accuracy at smooth regions and solid convergence. The new set of fully conservative 4th order central differencing[8, 9] have the same stencil width as the WENO schemes to facilitate the boundary condition treatment.

2 Numerical Methodology

The DDES of Spalart[2] is based on the Spalart-Allmaras one equation model. The 3D Navier-Stokes equations are solved using the recently developed low diffusion E-CUSP scheme[13], a 5th order WENO scheme[10, 11] for the inviscid flux and 4th order central differencing for viscous terms[8, 9]. The LDE scheme is simpler and more CPU efficient than the Roe scheme due to no matrix operation. An implicit unfactored Gauss-Seidel line iteration is used to achieve high convergence rate. The high-scalability parallel computing is used to save wall clock time[14].

2.1 Governing Equations

The governing equations for DES are the spatially filtered 3D time accurate compressible Navier-Stokes equations in generalized coordinates(ξ, η, ζ) and can be expressed as the following conservative form:

$$\frac{\partial \mathbf{Q}}{\partial t} + \frac{\partial \mathbf{E}}{\partial \xi} + \frac{\partial \mathbf{F}}{\partial \eta} + \frac{\partial \mathbf{G}}{\partial \zeta} = \frac{1}{Re}\left(\frac{\partial \mathbf{E}_v}{\partial \xi} + \frac{\partial \mathbf{F}_v}{\partial \eta} + \frac{\partial \mathbf{G}_v}{\partial \zeta}\right) + \mathbf{S} \tag{1}$$

where Re is the Reynolds number. DDES by Spalart et al.[2] is used to close the system of equations. The equations are nondimenisonalized based on airfoil chord L_∞, freestream density ρ_∞ and velocity U_∞.

The conservative variable vector $\mathbf{Q}$, the inviscid flux vectors $\mathbf{E}$, $\mathbf{F}$, $\mathbf{G}$, the viscous flux $\mathbf{E_v}$, $\mathbf{F_v}$, $\mathbf{G_v}$ and the source term vector $\mathbf{S}$ are expressed as

$$\mathbf{Q} = \frac{1}{J}\begin{pmatrix} \bar\rho \\ \bar\rho\tilde u \\ \bar\rho\tilde v \\ \bar\rho\tilde w \\ \bar\rho\tilde e \\ \bar\rho\tilde\nu_t \end{pmatrix}, \mathbf{E} = \begin{pmatrix} \bar\rho U \\ \bar\rho\tilde u U + l_x\bar p \\ \bar\rho\tilde v U + l_y\bar p \\ \bar\rho\tilde w U + l_z\bar p \\ (\bar\rho\tilde e + \bar p)\, U - l_t\bar p \\ \bar\rho\tilde\nu U \end{pmatrix}, \mathbf{F} = \begin{pmatrix} \bar\rho V \\ \bar\rho\tilde u V + m_x\bar p \\ \bar\rho\tilde v V + m_y\bar p \\ \bar\rho\tilde w V + m_z\bar p \\ (\bar\rho\tilde e + \bar p)\, V - m_t\bar p \\ \bar\rho\tilde\nu V \end{pmatrix}, \mathbf{G} = \begin{pmatrix} \bar\rho W \\ \bar\rho\tilde u W + n_x\bar p \\ \bar\rho\tilde v W + n_y\bar p \\ \bar\rho\tilde w W + n_z\bar p \\ (\bar\rho\tilde e + \bar p)\, W - n_t\bar p \\ \bar\rho\tilde\nu W \end{pmatrix} \tag{2}$$

$$\mathbf{E_v} = \begin{pmatrix} 0 \\ l_k\bar\tau_{xk} \\ l_k\bar\tau_{yk} \\ l_k\bar\tau_{zk} \\ l_k\left(\tilde u_i\bar\tau_{ki} - \bar q_k\right) \\ \frac{\bar\rho}{\sigma}\left(\nu + \tilde\nu\right)\left(\mathbf{l}\bullet\nabla\tilde\nu\right) \end{pmatrix}, \mathbf{F_v} = \begin{pmatrix} 0 \\ m_k\bar\tau u_{xk} \\ m_k\bar\tau_{yk} \\ m_k\bar\tau u_{zk} \\ m_k\left(\tilde u_i\bar\tau_{ki} - \bar q_k\right) \\ \frac{\bar\rho}{\sigma}\left(\nu + \tilde\nu\right)\left(\mathbf{m}\bullet\nabla\tilde\nu\right) \end{pmatrix}, \mathbf{G_v} = \begin{pmatrix} 0 \\ n_k\bar\tau_{xk} \\ n_k\bar\tau_{yk} \\ n_k\bar\tau_{zk} \\ n_k\left(\tilde u_i\bar\tau_{ki} - \bar q_k\right) \\ \frac{\bar\rho}{\sigma}\left(\nu + \tilde\nu\right)\left(\mathbf{n}\bullet\nabla\tilde\nu\right) \end{pmatrix} \tag{3}$$

$$\mathbf{S} = \frac{1}{J}\begin{pmatrix} 0 \\ 0 \\ 0 \\ 0 \\ 0 \\ S_\nu \end{pmatrix} \tag{4}$$

where ρ is the density, p is the static pressure, and e is the total energy per unit mass. The overbar denotes a regular filtered variable, and the tilde is used to denote the Favre filtered variable. ν is kinematic viscosity and $\tilde{\nu}$ is the working variable related to eddy viscosity in S-A model. U, V and W are the contravariant velocities in ξ, η, ζ directions, and defined as

$$\begin{array}{l} U = l_t + \mathbf{l} \bullet \mathbf{V} = l_t + l_x\tilde{u} + l_y\tilde{v} + l_z\tilde{w} \\ V = m_t + \mathbf{m} \bullet \mathbf{V} = m_t + m_x\tilde{u} + m_y\tilde{v} + m_z\tilde{w} \\ W = n_t + \mathbf{n} \bullet \mathbf{V} = n_t + n_x\tilde{u} + n_y\tilde{v} + n_z\tilde{w} \end{array} \tag{5}$$

where J is the Jacobian of the coordinate transformation. l_t, m_t and n_t are the components of the interface contravariant velocity of the control volume in ξ, η and ζ directions respectively. $\mathbf{l}$, $\mathbf{m}$ and $\mathbf{n}$ denote the normal vectors located at the centers of ξ, η and ζ interfaces of the control volume with their magnitudes equal to the surface areas and pointing to the directions of increasing ξ, η and ζ.

$$\mathbf{l} = \frac{\nabla\xi}{J},\ \mathbf{m} = \frac{\nabla\eta}{J},\ \mathbf{n} = \frac{\nabla\zeta}{J} \tag{6}$$

$$l_t = \frac{\xi_t}{J},\ m_t = \frac{\eta_t}{J},\ n_t = \frac{\zeta_t}{J} \tag{7}$$

The source term S_ν in Eq. (4), is given by

$$\begin{array}{l} S_\nu = \bar{\rho}C_{b1}\left(1 - f_{t2}\right)\tilde{S}\tilde{\nu} + \frac{1}{Re}\left[-\bar{\rho}\left(C_{w1}f_w - \frac{C_{b1}}{\kappa^2}f_{t2}\right)\left(\frac{\tilde{\nu}}{d}\right)^2\right. \\ \quad \left. + \frac{\bar{\rho}}{\sigma}C_{b2}\left(\nabla\tilde{\nu}\right)^2 - \frac{1}{\sigma}\left(\nu + \tilde{\nu}\right)\nabla\tilde{\nu} \bullet \nabla\bar{\rho}\right] + Re\left[\bar{\rho}f_{t1}\left(\Delta q\right)^2\right] \end{array} \tag{8}$$

where

$$\chi = \frac{\tilde{\nu}}{\nu}, \qquad f_{v1} = \frac{\chi^3}{\chi^3 + c_{v1}^3}, \qquad f_{v2} = 1 - \frac{\chi}{1 + \chi f_{v1}}, \qquad f_{t1} = C_{t1}g_t exp\left[-C_{t2}\frac{\omega_t^2}{\Delta U^2}\left(d^2 + g_t^2 d_t^2\right)\right] \tag{9}$$

$$f_{t2} = C_{t3}exp\left(-C_{t4}\chi^2\right), \qquad f_w = g(\frac{1 + c_{w3}^6}{g^6 + c_{w3}^6})^{1/6}, \qquad g = r + c_{w2}(r^6 - r) \tag{10}$$

$$g_t = min\left(0.1, \frac{\Delta q}{\omega_t \Delta x_t}\right), \qquad \tilde{S} = S + \frac{\tilde{\nu}}{k^2 d^2}f_{v2}, \qquad r = \frac{\tilde{\nu}}{\tilde{S}k^2 d^2} \tag{11}$$

where, ω_t is the wall vorticity at the wall boundary layer trip location, d is the distance to the closest wall, d_t is the distance of the field point to the trip location, Δq is the difference of the velocities between the field point and the trip location, Δx_t is the grid spacing along the wall at the trip location. The values of the coefficients are: $c_{b1} = 0.1355, c_{b2} = 0.622, \sigma = \frac{2}{3}, c_{w1} = \frac{c_{b1}}{k^2} + (1 + c_{b2})/\sigma, c_{w2} = 0.3, c_{w3} = 2, k = 0.41, c_{v1} = 7.1, c_{t1} = 1.0, c_{t2} = 2.0, c_{t3} = 1.1, c_{t4} = 2.0$.

The shear stress $\bar{\tau}_{ik}$ and total heat flux $\bar{q}_k$ in Cartesian coordinates is given by

$$\bar{\tau}_{ik} = (\mu + \mu_{DES})\left[\left(\frac{\partial\tilde{u}_i}{\partial x_k} + \frac{\partial\tilde{u}_k}{\partial x_i}\right) - \frac{2}{3}\delta_{ik}\frac{\partial\tilde{u}_j}{\partial x_j}\right] \tag{12}$$

$$\bar{q}_k = -\left(\frac{\mu}{Pr} + \frac{\mu_{DES}}{Pr_t}\right)\frac{\partial\tilde{T}}{\partial x_k} \tag{13}$$

where μ is from Sutherland's law, and $\mu_{DES}(= \bar{\rho}\tilde{\nu}f_{v1})$ is determined by the equation for the S-A model[15]. The above equations are in the tensor form, where the subscripts i, k represents the coordinates x, y, z and the Einstein summation convention is used. Eq.(12) and (13) are transformed to the generalized coordinate system in computation.

To overcome grid induced separation problem, the DDES model suggested by Spalart et al.[2] switches the subgrid scale formulation in S-A model as follows

$$\tilde{d} = d - f_d max(0, d - C_{DES}\Delta) \tag{14}$$

where

$$f_d = 1 - tanh([8r_d]^3) \tag{15}$$

$$r_d = \frac{\nu_t + \nu}{(U_{i,j}U_{i,j})^{0.5}k^2d^2} \tag{16}$$

where Δ is the largest spacing of the grid cell in all the directions. Within the boundary layer close to walls, $\tilde{d} = d$, and away from the boundary layer, $\tilde{d} = d - f_d max(0, d - C_{DES}\Delta)$ is most of the cases. This mechanism enables DDES to behave as a RANS model in the near-wall region, and LES away from walls. This modification in $\tilde{d}$ reduces the grey transition area between RANS and LES. The coefficient $C_{DES} = 0.65$ is used as set in the homogeneous turbulence[16]. The Pr_t may take the value of 0.9 within the boundary layer for RANS mode and 0.5 for LES mode away from the wall surface.

The equation of state as a constitutive equation relating density to pressure and temperature is defined as:

$$\bar{\rho}\tilde{e} = \frac{\bar{p}}{(\gamma - 1)} + \frac{1}{2}\bar{\rho}(\tilde{u}^2 + \tilde{v}^2 + \tilde{w}^2) \tag{17}$$

where γ is the ratio of specific heats. For simplicity, all the bar and tilde in above equations will be dropped in the rest of this paper.

2.2 Time Marching Scheme

The time dependent governing equation (1) is solved using dual time stepping method suggested by Jameson[17]. A pseudo temporal term $\frac{\partial Q}{\partial \tau}$ is added to the governing Eq. (1). This term vanishes at the end of each physical time step, and has no influence on the accuracy of the solution. An implicit pseudo time marching scheme using line Gauss-Seidel line relaxation is employed to achieve high convergence rate instead of using the explicit scheme as given by Jamesonin [18, 19]. The physical temporal term is discretized implicitly using a three point, backward differencing as the following:

$$\frac{\partial \mathbf{Q}}{\partial t} = \frac{3\mathbf{Q^{n+1}} - 4\mathbf{Q^n} + \mathbf{Q^{n-1}}}{2\Delta t} \tag{18}$$

where $n-1$, n and $n+1$ are three sequential time levels, which have a time interval of Δt. The first-order Euler scheme is used to discretize the pseudo temporal term. The semi-discretized equations of the governing equations are finally given as the following:

$$\begin{gathered}\left[\left(\tfrac{1}{\Delta\tau} + \tfrac{1.5}{\Delta t}\right) I - \left(\tfrac{\partial R}{\partial \mathbf{Q}}\right)^{n+1,m}\right] \delta\mathbf{Q^{n+1,m+1}} \\ = R^{n+1,m} - \tfrac{3\mathbf{Q^{n+1,m}} - 4\mathbf{Q^n} + \mathbf{Q^{n-1}}}{2\Delta t}\end{gathered} \tag{19}$$

where the $\Delta\tau$ is the pseudo time step, and R means the net flux determined by the spatial high order numerical schemes.

2.3 Approximate Riemann Solver[13]

The Low Diffusion E-CUSP (LDE) Scheme is used to evaluate the inviscid fluxes with the 5th order WENO scheme[10, 11]. The conservative variables are extrapolated to the cell interface as left(L) and right(R) values using the values on neighboring cells, then the inviscid fux are reconstructed based on these extrapolated variables. The basic idea of the LDE scheme is to split the inviscid flux into the convective flux E^c and the pressure flux E^p. With an extra equation from the S-A model for DDES, the splitting is basically the same as the original scheme for the Euler equation. This is an advantage over the Roe scheme[20], for which the eigenvectors need to be derived when any extra equation is added to the governing equations. In [21], the LDE scheme is shown to be more efficient than the Roe scheme when the S-A one equation turbulence model is coupled. In generalized coordinate system, the flux **E** can be split as the following:

$$\mathbf{E}' = E^c + E^p = \begin{pmatrix} \rho U \\ \rho u U \\ \rho v U \\ \rho w U \\ \rho e U \\ \rho \tilde{\nu} U \end{pmatrix} + \begin{pmatrix} 0 \\ l_x p \\ l_y p \\ l_z p \\ p\overline{U} \\ 0 \end{pmatrix} \tag{20}$$

where, U is the contravariant velocity in ξ direction and is defined as the following:

$$U = l_t + l_x u + l_y v + l_z w \tag{21}$$

$\overline{U}$ is defined as:

$$\overline{U} = l_x u + l_y v + l_z w \tag{22}$$

The convective term, E^c is evaluated by

$$E^c = \rho U \begin{pmatrix} 1 \\ u \\ v \\ w \\ e \\ \tilde{\nu} \end{pmatrix} = \rho U f^c, \; f^c = \begin{pmatrix} 1 \\ u \\ v \\ w \\ e \\ \tilde{\nu} \end{pmatrix} \tag{23}$$

let

$$C = c\left(l_x^2 + l_y^2 + l_z^2\right)^{\frac{1}{2}} \tag{24}$$

where $c = \sqrt{\gamma R T}$ is the speed of sound.

Then the convective flux at interface $i + \frac{1}{2}$ is evaluated as:

$$E^c_{i+\frac{1}{2}} = C_{\frac{1}{2}}\left[\rho_L C^+ f^c_L + \rho_R C^- f^c_R\right] \tag{25}$$

where, the subscripts L and R represent the left and right hand sides of the interface. The Mach number splitting of Edwards[22] is borrowed to determine c^+ and c^- as the following:

$$\begin{aligned}
&C_{\frac{1}{2}} = \tfrac{1}{2}\left(C_L + C_R\right) \\
&C^+ = \alpha_L^+\left(1 + \beta_L\right) M_L - \beta_L M_L^+ - M_{\frac{1}{2}}^+ \\
&C^- = \alpha_R^-\left(1 + \beta_R\right) M_R - \beta_R M_R^- + M_{\frac{1}{2}}^- \\
&M_L = \tfrac{U_L}{C_{\frac{1}{2}}}, \; M_R = \tfrac{U_R}{C_{\frac{1}{2}}} \\
&\alpha_{L,R} = \tfrac{1}{2}\left[1 \pm sign\left(M_{L,R}\right)\right] \\
&\beta_{L,R} = -max\left[0, 1 - int\left(\left|M_{L,R}\right|\right)\right] \\
&M_{\frac{1}{2}}^+ = M_{\frac{1}{2}} \tfrac{C_R + C_L \Phi}{C_R + C_L}, \; M_{\frac{1}{2}}^- = M_{\frac{1}{2}} \tfrac{C_L + C_R \Phi^{-1}}{C_R + C_L} \\
&\Phi = \tfrac{\left(\rho C^2\right)_R}{\left(\rho C^2\right)_L} \\
&M_{\frac{1}{2}} = \beta_L \delta^+ M_L^- - \beta_R \delta^- M_R^+ \\
&M_{L,R}^{\pm} = \pm\tfrac{1}{4}\left(M_{L,R} \pm 1\right)^2 \\
&\delta^{\pm} = \tfrac{1}{2}\left\{1 \pm sign\left[\tfrac{1}{2}\left(M_L + M_R\right)\right]\right\}
\end{aligned} \tag{26}$$

The pressure flux, E^p is evaluated as the following

$$E^p_{i+\frac{1}{2}} = \begin{pmatrix} 0 \\ \mathcal{P}^+ p\, l_x \\ \mathcal{P}^+ p\, l_y \\ \mathcal{P}^+ p\, l_z \\ \frac{1}{2} p \left[\overline{U} + \overline{C}_{\frac{1}{2}} \right] \\ 0 \end{pmatrix}_L + \begin{pmatrix} 0 \\ \mathcal{P}^- p\, l_x \\ \mathcal{P}^- p\, l_y \\ \mathcal{P}^- p\, l_z \\ \frac{1}{2} p \left[\overline{U} - \overline{C}_{\frac{1}{2}} \right] \\ 0 \end{pmatrix}_R \tag{27}$$

The contravariant speed of sound $\overline{C}$ in the pressure vector is consistent with $\overline{U}$. It is computed based on C as the following,

$$\overline{C} = C - l_t \tag{28}$$

The use of $\overline{U}$ and $\overline{C}$ instead of U and C in the pressure vector is to take into account of the grid speed so that the flux will transit from subsonic to supersonic smoothly. When the grid is stationary, $l_t = 0$, $\overline{C} = C$, $\overline{U} = U$.

The pressure splitting coefficient is:

$$\mathcal{P}^{\pm}_{L,R} = \frac{1}{4} \left(M_{L,R} \pm 1 \right)^2 \left(2 \mp M_L \right) \tag{29}$$

The LDE scheme can capture crisp shock profile and exact contact surface discontinuities as accurately as the Roe scheme[13]. However, it is simpler and more CPU efficient than the Roe scheme due to no matrix operation.

2.4 The 5th Order WENO Scheme [10, 11]

The interface flux, $E_{i+\frac{1}{2}} = E(Q_L, Q_R)$, is evaluated by determining the conservative variables Q_L and Q_R using fifth-order WENO scheme. For example,

$$(Q_L)_{i+\frac{1}{2}} = \omega_0 q_0 + \omega_1 q_1 + \omega_2 q_2 \tag{30}$$

where

$$\begin{aligned} q_0 &= \tfrac{1}{3} Q_{i-2} - \tfrac{7}{6} Q_{i-1} + \tfrac{11}{6} Q_i \\ q_1 &= -\tfrac{1}{6} Q_{i-1} + \tfrac{5}{6} Q_i + \tfrac{1}{3} Q_{i+1} \\ q_2 &= \tfrac{1}{3} Q_i + \tfrac{5}{6} Q_{i+1} - \tfrac{1}{6} Q_{i+2} \end{aligned} \tag{31}$$

$$\omega_k = \frac{\alpha_k}{\alpha_0 + \ldots + \alpha_{r-1}} \tag{32}$$

$$\begin{aligned} &\alpha_k = \tfrac{C_k}{\epsilon + IS_k},\ k = 0, \ldots, r-1 \\ &C_0 = 0.1,\ C_1 = 0.6,\ C_2 = 0.3 \\ &IS_0 = \tfrac{13}{12} \left(Q_{i-2} - 2Q_{i-1} + Q_i \right)^2 + \\ &\qquad \tfrac{1}{4} \left(Q_{i-2} - 4Q_{i-1} + 3Q_i \right)^2 \\ &IS_1 = \tfrac{13}{12} \left(Q_{i-1} - 2Q_i + Q_{i+1} \right)^2 + \tfrac{1}{4} \left(Q_{i-1} - Q_{i+1} \right)^2 \\ &IS_2 = \tfrac{13}{12} \left(Q_i - 2Q_{i+1} + Q_{i+2} \right)^2 + \\ &\qquad \tfrac{1}{4} \left(3Q_i - 4Q_{i+1} + Q_{i+2} \right)^2 \end{aligned} \tag{33}$$

where, ϵ is originally introduced to avoid the denominator becoming zero and is supposed to be a very small number. In [18], it is observed that IS_k will oscillate if ϵ is too small and also shift the weights away from the optimal values in the smooth region. The higher the ϵ values, the closer the weights approach the optimal values, C_k, which will give the symmetric evaluation of the interface flux with minimum numerical dissipation. When there are shocks in the flow field, ϵ can not be too large to maintain the sensitivity to shocks. In [18], $\epsilon = 10^{-2}$ is recommended for the transonic flow with shock waves. In this paper, since there is no shock in the flow, the $\epsilon = 0.3$ is used.

3 Boundary Conditions

Steady state freestream conditions are used for the upstream portion of the outer boundary. For downstream boundary, the static pressure was specified as freestream value, and the streamwise gradients of other variables were forced to vanish. The periodic boundary condition is used in spanwise direction. The wall treatment suggested in [18] to achieve flux conservation by shifting half interval of the mesh on the wall is employed. The no slip condition is employed on the surface, for computing the flux $F_{1/2}$ on the wall, there is

$$\mathbf{F_w} = \begin{pmatrix} \rho V \\ \rho u V + p\eta_x \\ \rho v V + p\eta_y \\ \rho w V + p\eta_z \\ (\rho e + p)V \end{pmatrix}_w = \begin{pmatrix} 0 \\ p\eta_x \\ p\eta_y \\ p\eta_z \\ 0 \end{pmatrix}_w$$

and a third-order accuracy wall boundary formula is used to evaluate $p|_w$,

$$p_w = \frac{1}{6}(11p_1 - 7p_2 + 2p_3)$$

4 Results and Discussion

4.1 Flat-Plate Boundary Layer

A defect of DES97 is an abnormal reaction to the excessive refinement of grid in the wall-parallel direction. This deficiency known as MSD originates from the intermediate region between RANS and LES domains of DES. Spalart et al. [2] suggested the Delayed DES which has a simple remedy in order to avoid MSD by re-defining the length scale of DES using the delayed LES function, $f_d = 1 - tanh(8[r_d]^3)$. Before the stalled NACA 0012 airfoil simulation, the test of DDES behavior in the thin flat plate boundary layer was performed in the same manner as done by Spalart et al.[2]. In their report, the eddy viscosity of DES is reduced by about 75%[2] compared with DDES for a turbulent boundary layer on a 3D flat plate.

The computational mesh for the flat plate shown in Fig. 1 is constructed to have the grid spacing(Δ) parallel to the wall less than the turbulent boundary layer thickness, $\delta(= 0.37(Re_L)^{-0.2}L)$[23]. The grid has y^+ less than unity. Re_x of 1.2×10^7 and Re_z of 1.8×10^4 are applied based on unit Reynolds number(Re_L) of 1×10^6. The grid used in this study has the wall-parallel grid spacing about 1/10th of its thickness($\Delta x \approx \Delta z \approx 0.1\delta$), and the fine grid starts at 10 times of unit length(L). This grid is defined as the "severe grid" by Spalart et al. to test the DDES model. The Mach number used for this case is in the incompressible range at 0.1 and the Reynolds number based on the plate length is 12×10^6.

Fig. 2 shows the turbulent boundary layer profile from RANS, DES97 and DDES. Good agreement with the law of the wall is achieved even with the severe grid. DDES behavior in the flat boundary layer is presented in Fig. 3. DES shows the reduction of its peak eddy viscosity by about 65%, while with DDES the eddy viscosity is almost fully preserved. Compared to Spalart's results, the DES conducted in this paper achieved higher peak eddy viscosity even though it is substantially lower that that of DDES. That may be because DES solution is highly dependent on the grid and the present grid is not exactly the same as that of Spalart et al. due to lacking their grid information.

Fig. 4 shows $u/U_\infty, r_d, f_d$ predicted by DDES. It is shown that f_d function gradually changes from 0 to 1 within the boundary layer. Note that f_d is designed to be 1 in the LES region, where $r_d << 1$. All these results show that the DDES is correctly implemented and achieves the goal to remove the MSD problem of DES97.

4.2 NACA0012 Dynamic Stall

Simulation of the NACA0012 aerodynamic stall flows at 45° angle of attack is carried out to validate simulation capability of DDES. Reynolds number of 1.3×10^6, Mach number of 0.5, and airfoil span length of 1 chord are used based on the experiment of the NACA0012 airfoil[24, 25].

The 3D mesh is constructed using the O-mesh topology since O-grids can minimize mesh skewness near the airfoil wall. Two different grids using mesh A($145 \times 81 \times 21$) and mesh B($193 \times 101 \times 31$) are used for the mesh refinement test. Fig. 5 shows mesh B that consists of 193 nodes around airfoil, 31 nodes in the spanwise direction, and 101 nodes in the direction of normal to the wall. The $1st$ grid spacing on the surface is determined as y^+ is less than 1. The boundary is located about 54 times of the airfoil chord, which is large enough to avoid wave reflection.

The unsteady simulations is started from a uniform initial flow and is performed over dimensionless time 200 with a pseudo time CFL number of 3. To avoid the transitional flow effect, the results are started to record at time level of 25. The number of pseudo time steps per each physical time step is determined by applying the convergence criteria 1×10^{-10}, which is usually achieved within 60 iterations. Physical time step of 0.02 is used.

Fig. 6 represents the predicted drag coefficients(C_D) from mesh refinement test. The URANS predicts a phase clocked sinusoidal oscillation due to vortex shedding. Drag coefficients predicted by DES and DDES oscillate in an more irregular manner. The URANS simulation is very well converged based on mesh size. The DES and DDES are also converged to the same statistics level.

Fig. 7 compares drag coefficients by URANS, DES and DDES. The URANS over-predicts the time averaged drag by 33.6%, whereas the DES and DDES predict the drag in good agreement with the experiment. Time averaged drag coefficients are compared with experiment in Fig. 8. Average values were obtained from $25T$ to over $200T$. C_D of experiment is 1.075. The average of URANS, DES and DDES are 1.437, 1.074, and 1.076 respectively. URANS overpredicted by about 33.6%, while DES and DDES show high accuracy in the predction of drag less than 0.1% compared to experiment.

Fig. 9 and Fig. 10 display the instantaneous vorticity contours of 50% span at non-dimensional time $100T$ and $200T$. URANS captures the phase locked vortex shedding that usually occurs at low Reynolds number flow, while DDES and DES shows more realistic and turbulent vortical flow structures in the regions of massive separations. As expected, DES shows more chaotic flow motion than URANS. Flow separation occurs on the upper surface near leading edge as shown by the vorticity streaks.

Distributions of surface isentropic Mach number of 50% span are shown in Fig. 11. A small pressure gradient exists along the span even for URANS. Fig. 12 shows velocity contours of 50% span in the spanwise direction. In addition to the very different vortex structures as aforementioned, Fig. 12 also indicates that the URANS predicts the wake dissipating faster than the DES and DDES.

Fig. 13 shows velocity vector of 50% span colored with static pressure around flow separation point. Separation takes place at about same point where adverse pressure gradient appears for all cases. Fig. 14 shows Mach number contours of 50% span. Both DES and DDES demonstrate that the large structure of vortical flow develops downstream with samm eddies behind airfoil and with no shocks. Fig. 15 shows 3D vortex trajectories behind airfoil predicted by URANS, DES and DDES. DES and DDES capture the massively separated flow in more LES-like manner, while URANS simulates the vortex like a large 2D flow separation.

5 Conclusions

Numerical simulation of a stall flow over a NACA0012 airfoil at 45° angle of attack was performed using URANS, DES and Delayed DES of turbulence. The DDES is validated for a flat-plate turbulent boundary layer using a severe grid designed to generate Modeled-Stress Depletion of DES. DES shows 65% reduction of the eddy viscosity in the wall boundary layer, while DDES preserves almost fully the eddy viscosity.

For the stalled NACA0012 airflil flow, DDES demonstrates an excellent capability to simulate aerodynamic stall. The predicted drag coefficient for the NACA0012 aerodynamic stall is 1.07 by both DDES and DES, which agree excellently with experiment. URANS overestimated C_d by 33.6% compared with the experiment. The URANS predicts a phase clocked sinusoidal oscillation due to vortex shedding, whereas the DDES and DES predict the vortex structures in a more chaotic manner. Fig. 15 shows 3D vortex trajectories predicted by URANS, DES and DDES. DDES and DES shows more realistic stalled flow.

Acknowledgement

This research is supported by the funding of Air Force Research Lab under GUIde Consortium grant 09-GUIDE-1010.

References

[1] P.R. Spalart, W.H. Jou, M. Strelets, and S.R. Allmaras, “Comments on the Feasibility of LES for Wings, and on a Hybrid RANS/LES Approach.” Advances in DNS/LES, 1st AFOSR Int. Conf. on DNS/LES, Greyden Press, Columbus, H., Aug. 4-8, 1997.

[2] P.R. Spalart, S. Deck, M. Shur, and K.D. Squires, “A New Version of Detached-Eddy Simulation, Resistant to Ambiguous Grid Densities,” *Theoritical and Computational Fluid Dynamics*, vol. 20, pp. 181–195, 2006.

[3] F.R. Menter, and M. Kuntz, “Adaptation of Eddy-Viscosity Turbulence Models to Unsteady Separated Flow Behind Vehilces, *The Aerodynamics of Heavy Vehicles: Trucks, Buses and Trains, Edited by McCallen, R. Browand, F. and Ross, J. ,” Springer, Berlin Heidelberg New York, 2004*, 2-6 Dec. 2002.

[4] K. S. R. C. S.A. Morton, J.R. Forsythe, “Detached-Eddy Simulations of Full Aircraft Experincing Massively Separated Flows.” The 5th Asian Computational Fluid Dynamics Conference, Busan, Korea, October 27 - 30, 2003.

[5] Y. H. G. H. G. Martinat, M. Braza, “Turbulence Modelling of the Flow Past a Pitching NACA0012 Airfoil at $10^5$and 10^7 Reynolds Numbers,” *J. of Fluids and Structures*, vol. 24, pp. 1294–1303, 2008.

[6] M. R. S. Moreau, J. Christopher, “LES of the Trailing-edge Flow and Noise of a NACA0012 Airfoil Near Stall.” Proceedings of the Summer Program 2008, Center for Turbulence Research, 2008.

[7] P. S. A.K. Travin, M.L. Shur and M. Strelets, “Improvement of delayed Detached Eddy Simulation for LES With Wall Modelling.” European Conference on Computational Fluid Dynamics, ECCOMAS CFD 2006, 2006.

[8] Y.-Q. Shen and G.-C. Zha, “Large Eddy Simulation Using a New Set of Sixth Order Schemes for Compressible Viscous Terms,” *Journal of Computational Physics*, vol. 229, pp. 8296–8312, 2010.

[9] G.-C. Z. Y.-Q. Shen and X. Chen, “High Order Conservative Differencing for Viscous Terms and the Application to Vortex-Induced Vibration Flows,” *Journal of Computational Physics*, vol. 228(2), pp. 8283–8300, 2009.

[10] Y.-Q. Shen and G.-C. Zha, “Improvement of the WENO Scheme Smoothness Estimator,” *International Journal for Numerical Methods in Fluids*, vol. DOI:10.1002/fld.2186, 2009.

[11] G.-C. Z. Y.-Q. Shen and B.-Y. Wang, “Improvement of Stability and Accuracy of Implicit WENO Scheme,” *AIAA Journal*, vol. 47, pp. 331–334, 2009.

[12] G. Jiang and C. Shu, “Efficient Implementation of Weighted ENO Schemes,” *Journal of Computational Physics*, vol. 126, pp. 202–228, 1996.

[13] G.C. Zha, Y.Q. Shen, and B.Y. Wang, “Calculation of Transonic Flows Using WENO Method with a Low Diffusion E-CUSP Upwind Scheme.” AIAA Paper 2008-0745, 46th AIAA Aerospace Sciences Meeting, Reno, NV, Jan. 2008.

[14] B.Y. Wang, and G.C. Zha, “ Detached Eddy Simulations of a Circular Cylinder Using a Low Diffusion E-CUSP and High-Order WENO Scheme.” AIAA Paper 2008-3855, AIAA 38th Fluid Dynamics Conference, Seattle, Washington, June 23-26, 2008.

[15] P.R. Spalart, and S.R. Allmaras, “A One-equation Turbulence Model for Aerodynamic Flows.” AIAA-92-0439, 1992.

[16] M. Shur, P.R. Spalart, M. Strelets, and A. Travin, “Detached-Eddy Simulation of an Airfoil at High Angle of Attack”, 4th Int. Symp. Eng. Turb. Modelling and Measurements, Corsica.” May 24-26, 1999.

[17] A. Jameson, “Time Dependent Calculations Using Multigrid with Applications to Unsteady Flows Past Airfoils and Wings.” AIAA Paper 91-1596, 1991.

[18] Y.Q. Shen, B.Y. Wang, and G.C. Zha, “Implicit WENO Scheme and High Order Viscous Formulas for Compressible Flows .” AIAA Paper 2007-4431, 2007.

[19] B. Y. W. Y. Q. Shen, “Improvement of Stability and Accuracy of Implicit WENO Scheme,” *AIAA Journal*, vol. 47, pp. 331–344, 2009.

[20] P. Roe, "Approximate Riemann Solvers, Parameter Vectors, and Difference Schemes," *Journal of Computational Physics*, vol. 43, pp. 357–372, 1981.

[21] B.Y. Wang, and G.C. Zha, "Comparison of a Low Diffusion E-CUSP and the Roe Scheme for RANS Calculation." AIAA Paper 2008-0596, 46th AIAA Aerospace Sciences Meeting and Exhibit, Jan. 7-10, 2008.

[22] J. Edwards, "A Low-Diffusion Flux-Splitting Scheme for Navier-Stokes Calculations," *Computer* & *Fluids*, vol. 6, pp. 635–659, 1997.

[23] H. schlichting, "Boundary Layer Theory." McGRAW-Hill, 1979.

[24] L. Loftin, "Airfoil Section Characteristics at High Angles of Attack." NASA TM 100019, October 1987.

[25] W. McCroskey, "A Critical Assessment of Wind Tunnel Results for the NACA0012 Airfoil." NACA TN 3241, August, 1954.

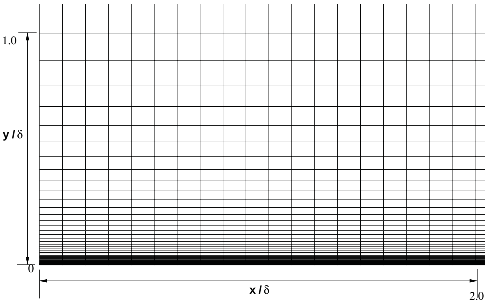

Figure 1: View of severe flat plate mesh with unit Reynolds number of 1×10^6; $\Delta x \approx \Delta z \approx 0.1\delta$

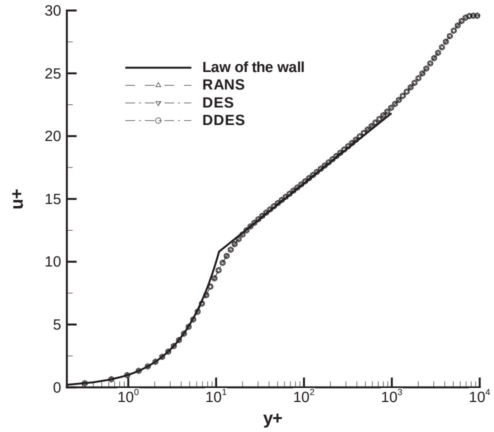

Figure 2: Predicted velocity profiles in the flat plate turbulent boundary layer

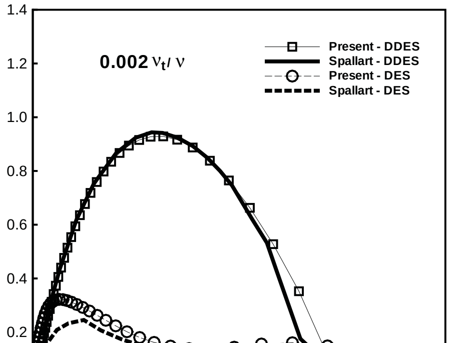

Figure 3: Distributions of $0.002\frac{\nu_t}{\nu}$ in the flat plate boundary layer; $\Delta_{\|} = 0.1\delta$

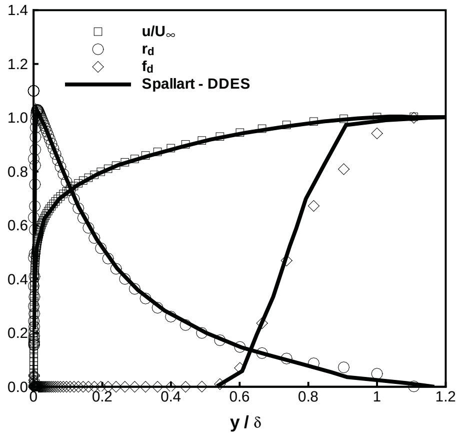

Figure 4: Distributions of $u/U_\infty, r_d, f_d$ in the flat plate boundary layer

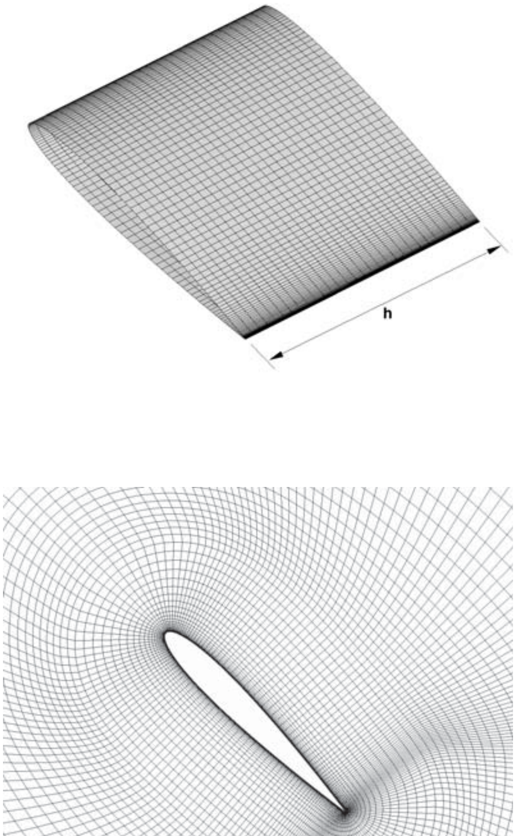

Figure 5: 3D O-mesh for NACA0012 airfoil at 45° AOA; $193 \times 101 \times 31$, R=56c, h=1c, $d_n = 1.0 \times 10^{-5}c$, $\Delta z/c = 0.033$

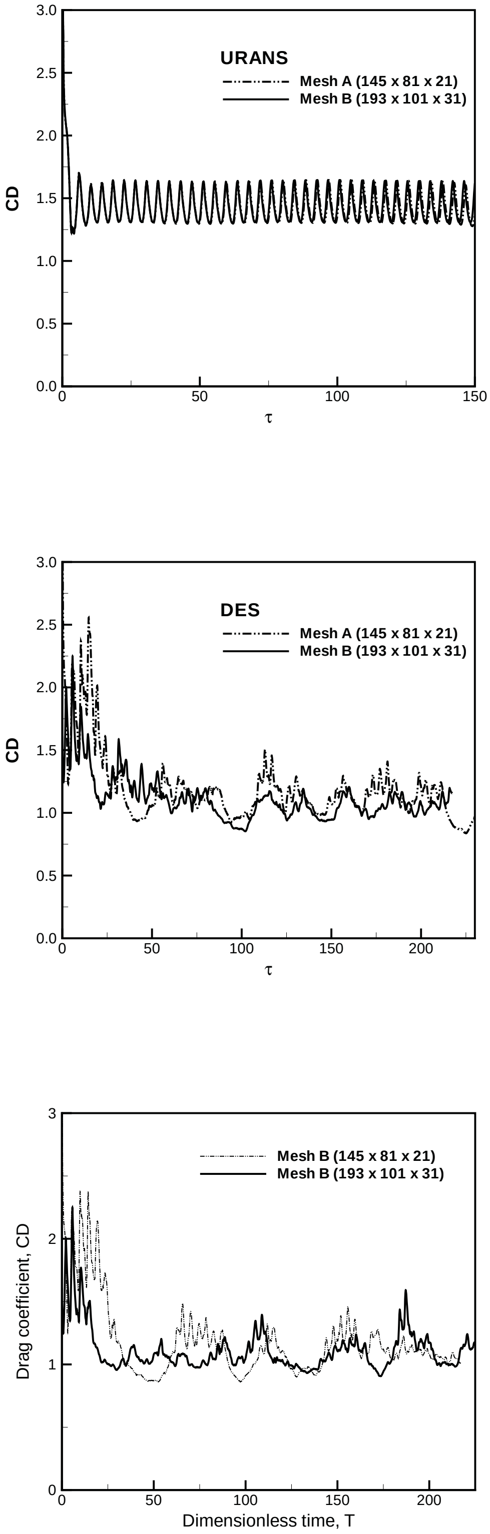

Figure 6: Drag coefficients by mesh refinement test

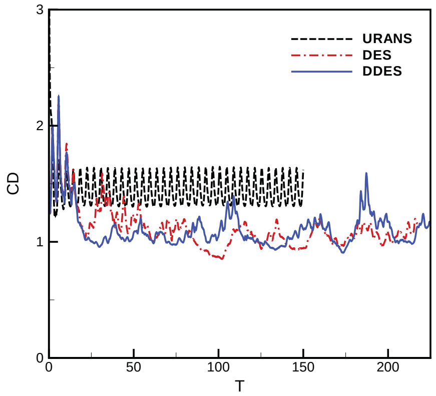

Figure 7: Comparison of drag coefficients from URANS, DES and DDES

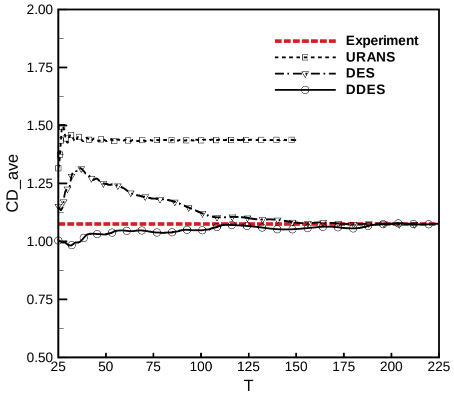

Figure 8: Time averaged drag coefficients

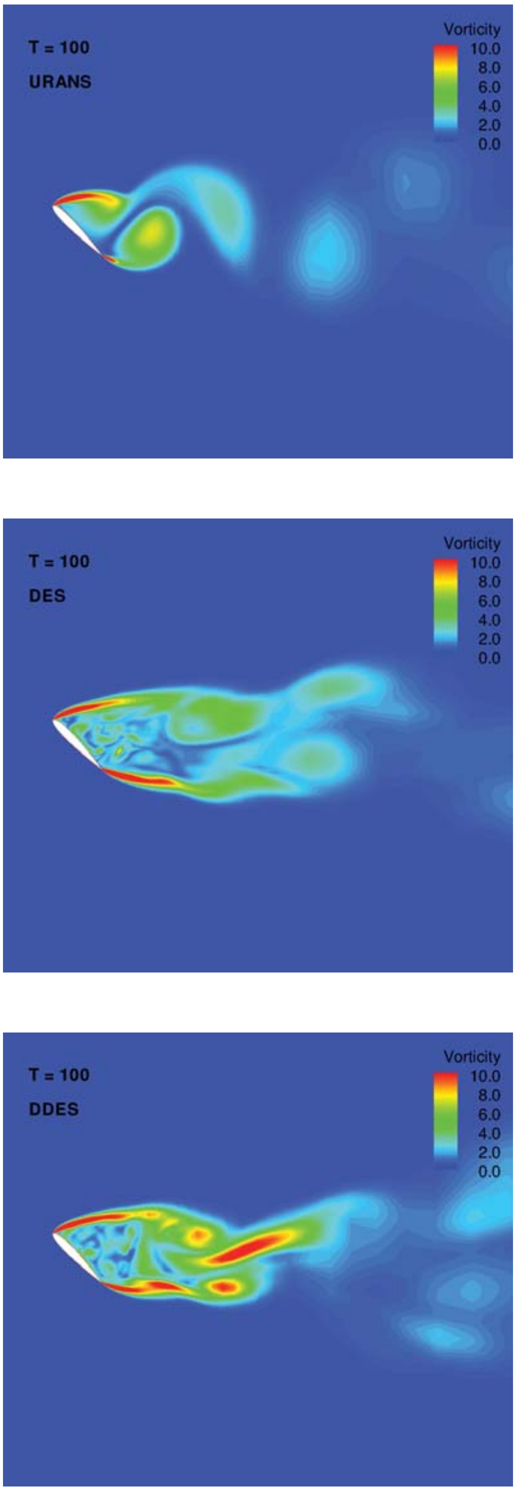

Figure 9: Vorticity contours of 50% span at $T = 100$

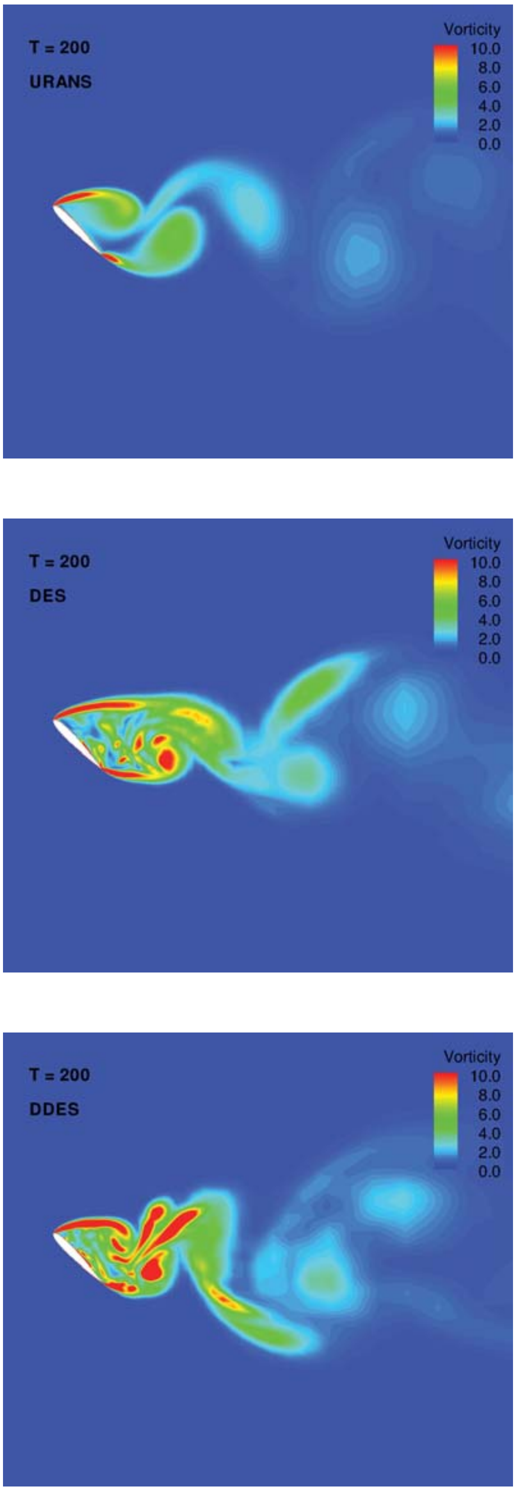

Figure 10: Vorticity contours of 50% span at $T = 200$

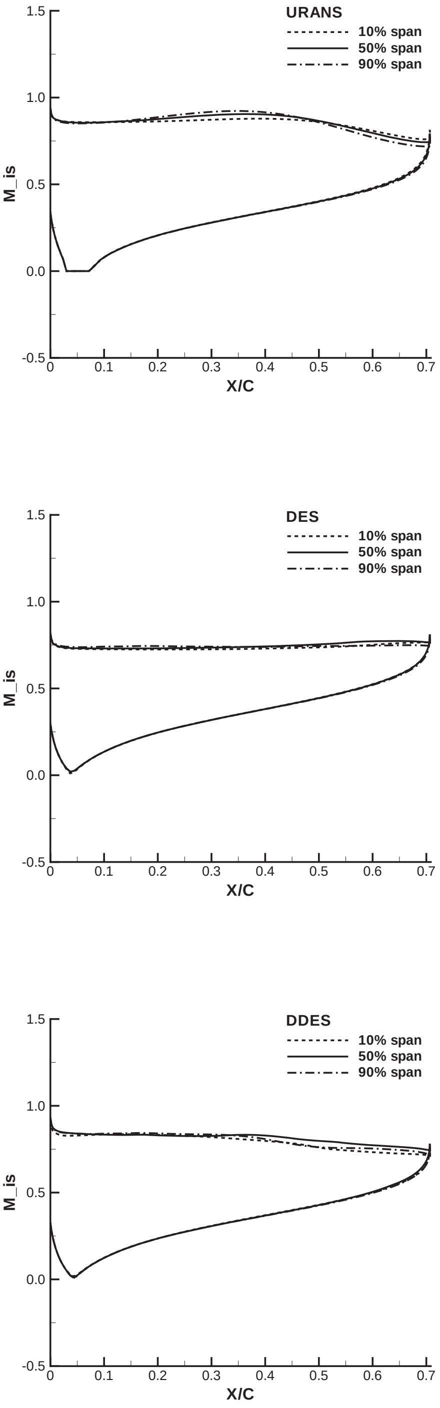

Figure 11: Surface isentropic Mach number(Ma_{is}) distributions of $10\%, 50\%, 90\%$ span at $T = 200$

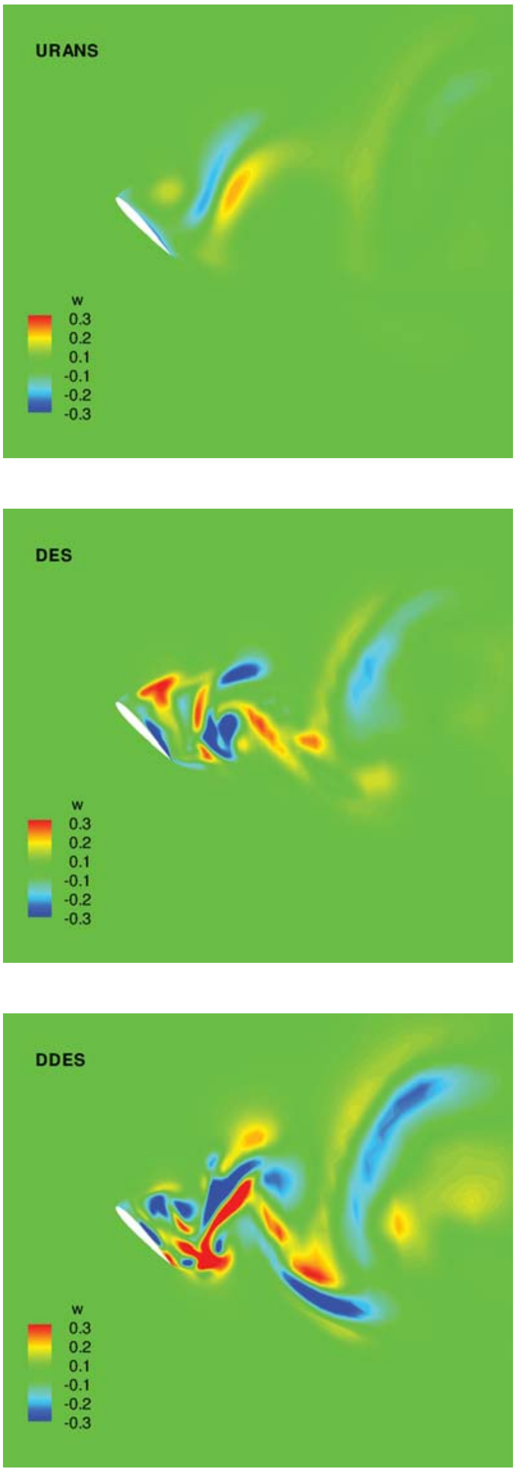

Figure 12: Spanwise velocity contours of 50% span at $T = 200$

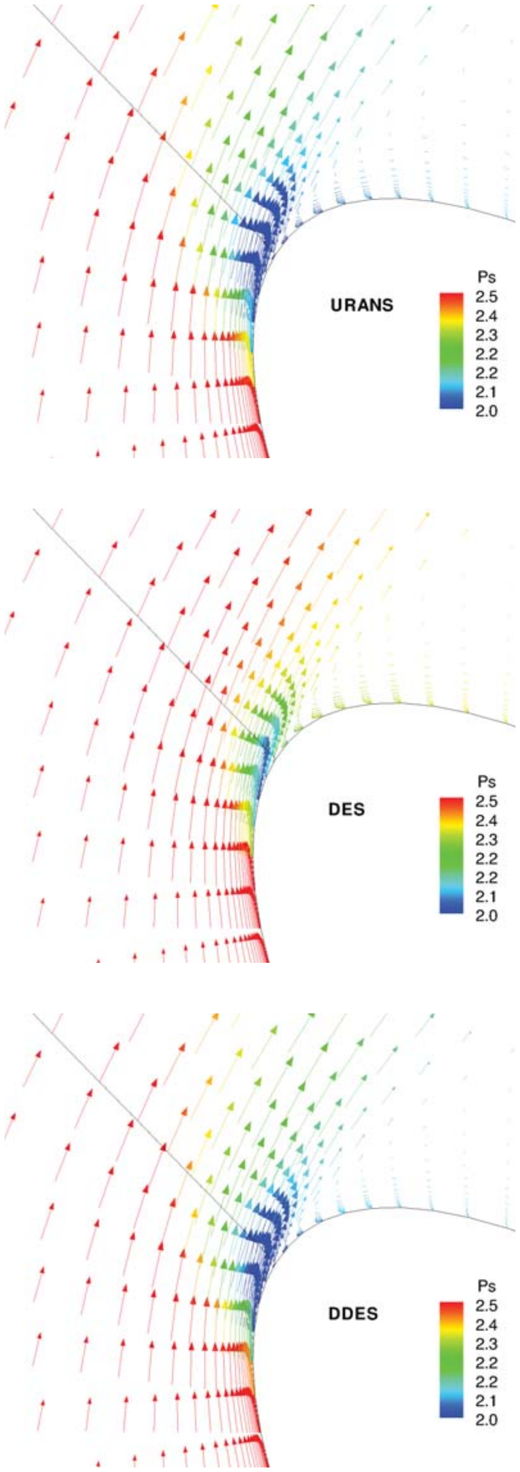

Figure 13: Velocity vector near leading edge flow separation point of 50% span at $T = 200$

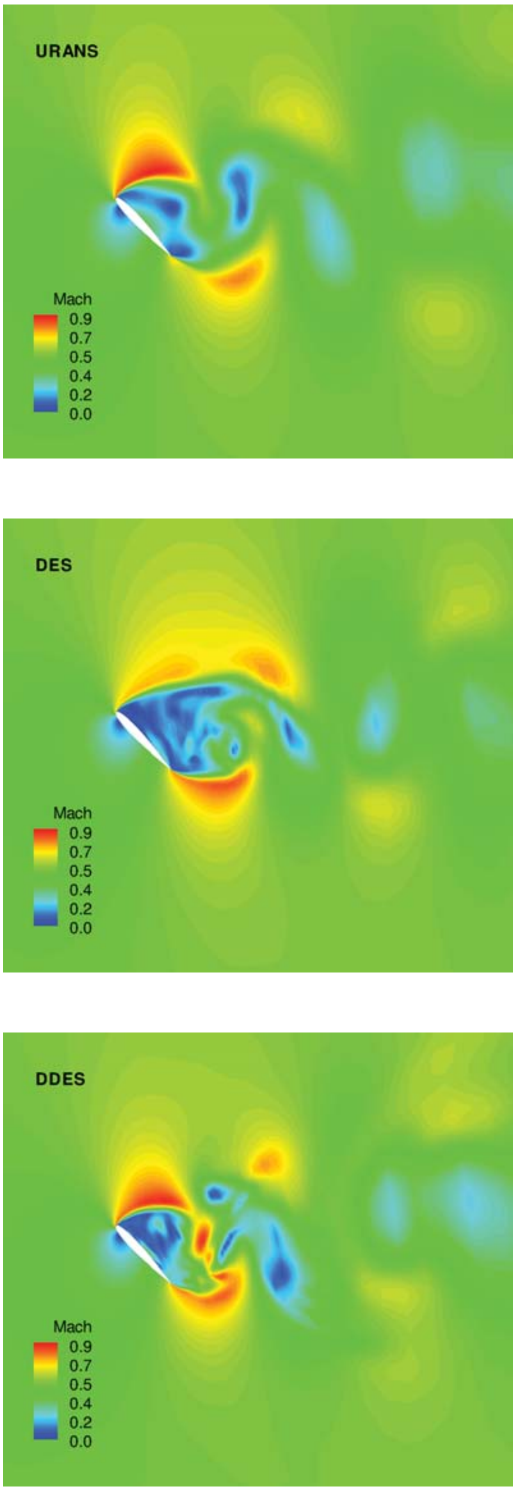

Figure 14: Mach number contours of 50% span at $T = 200$

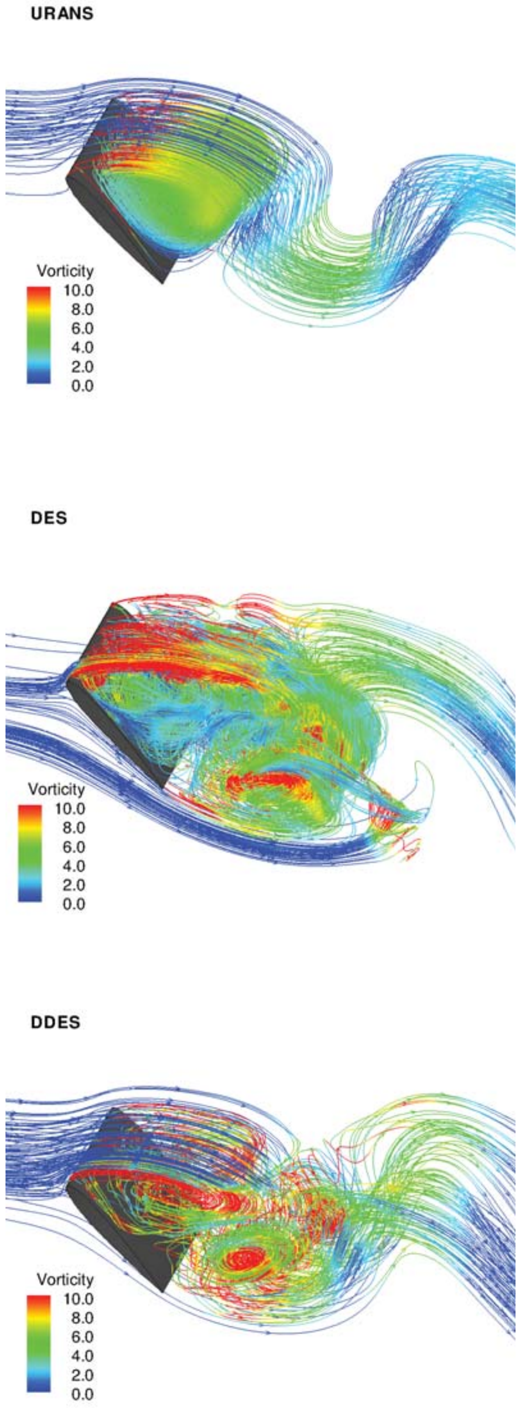

Figure 15: Vortex trajectories colored with vorticity at $T = 200$